https://doi.org/10.5194/egusphere-2026-1948
Preprint. Discussion started: 8 May 2026

The impact of pre-existing weaknesses on strike-slip fault evolution: insight into strain partitioning of the 2019 Ridgecrest earthquake

Christ F. Ramos Sánchez[1], Michele L. Cooke[1]

[1]Department of Earth, Geographic and Climate Sciences, University of Massachusetts Amherst, Amherst, 01003, USA

Correspondence to: Michele L. Cooke (cooke@umass.edu)

Abstract. The 2019 Ridgecrest mainshock produced a complex rupture pattern at the northwest end of the dextral rupture where a set of disconnected pre-existing faults that trend perpendicular to the strike of the mainshock fault had sinistral slip. This highly segmented geometry of active faulting may reflect immature faulting that provides insights into the early development of strike-slip faults. Physical experiments that simulate upper crustal deformation using scaled analogue materials, such as wet kaolin, allow us to control loading and material rheology, and directly document the complete evolution of strike-slip fault systems that grow in material with pre-existing weaknesses. To assess the impact of pre-existing weaknesses on strike-slip fault evolution we vary initial orientation and spacing of the vertical surfaces, and nature of basal shear loading (localized and distributed). Weaknesses oriented 60˚ and 90˚ from the applied dextral loading showed negligible slip while weaknesses oriented 120˚ developed sinistral slip and weaknesses oriented 150˚ had dextral slip. Experiments that developed sinistral slip along cross-faults (120˚) also showed distributed dextral strain between the faults that contributed to significant rotation of material, including the cross-faults, within the shear zone. When the sinistral faults were rotated to orientations unfavourable for continued slip, new dextral faults developed. This finding suggests that strike-slip systems with active cross faults represent immature stages of evolution that will become reorganized upon further strain accumulation. The amount of off-fault deformation and shear zone width depends on the presence of pre-existing weaknesses (even if they had low slip) and the persistence of fault irregularities that arose from slip along and interaction of new faults with the pre-existing weaknesses. Understanding how the orientation of pre-existing weaknesses influences the early evolution of strike-slip faults and strain localization over geologic time scales can inform future seismic hazard assessments of regions with pre-existing structures.

1 Introduction

The Eastern California Shear Zone of Southern California, USA, has hosted several historic ground rupturing earthquakes along complex networks of strike-slip faults . Rather than displaying continuous rupture surfaces, the active fault traces of these recent earthquakes in the Eastern California Shear Zone have multiple fault segments that include step overs and bends as well as a wide range of active fault orientations (Fialko and Jin, 2021; Platt and Becker, 2013). A contributing factor to the geometric complexity of these rupture traces is that they follow pre-existing faults and heterogeneities in the upper crust (e.g., Nevitt et al., 2023). The 2019 M 7.4 Ridgecrest earthquake produced a complex rupture pattern along the mainshock fault

https://doi.org/10.5194/egusphere-2026-1948
Preprint. Discussion started: 8 May 2026

where the northwest end of the dextral (right-lateral) rupture re-activated with sinistral (left-lateral) slip an array of cross-faults perpendicular to the strike of the mainshock fault (Figure 1; e.g., Antoine et al., 2021; Milliner et al., 2021). The highly segmented and disconnected geometry of active faulting at the northwest end of the rupture is believed to reflect very immature faulting (Antoine et al., 2021; Milliner et al., 2021) that can provide insight into the early development of strike-slip faults. Outcrops that preserve early stages of strike-slip fault evolution show evidence of early slip along pre-existing structures that may be followed by fault growth and linkage (e.g., Crider and Peacock, 2004). Because some orientations of pre-existing weakness will be more or less favourable for slip within the shear zone (e.g., Davis et al., 2000), the evolution of strike-slip faults depends on the orientation of any pre-existing weaknesses.

Understanding how the orientation of pre-existing weaknesses can influence the early evolution of strike-slip faults and strain localization can inform future seismic hazard assessments of regions with pre-existing structures. Using physical experiments that simulate upper crustal deformation with scaled crustal analogue materials, such as wet kaolin, we can control the experimental conditions (loading and material rheology) and we can directly document the complete emergent evolution of strike-slip fault systems (e.g., Dooley and Schreurs, 2012; González-Muñoz et al., 2024; Hatem et al., 2017; Reber et al., 2020). Such detailed temporal and spatial documentation of evolving active fault geometry and strain partitioning is not possible from field data, which only shows the cumulative result of deformation at available exposures. By tracking active fault geometry and off-fault deformation during experiments of strike-slip fault evolution, we gather information that may guide interpretations of crustal strike-slip fault evolution in the presence of pre-existing weaknesses.

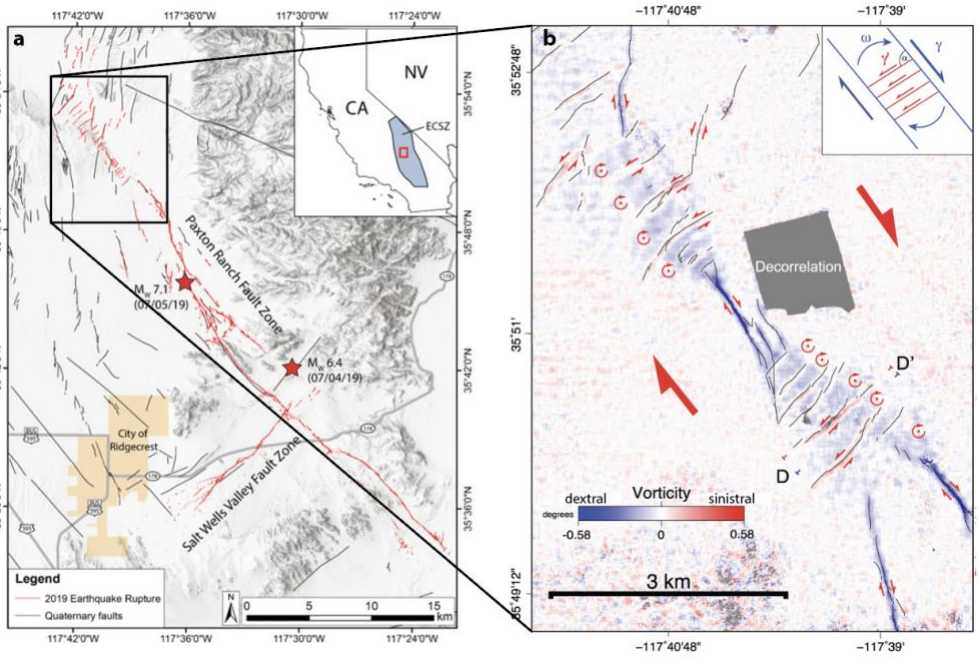

Figure 1. a. Ridgecrest foreshock and main shock rupture map (taken from Rosa et al., 2024). b. Coseismic slip and strain along the northwestern portion of the Ridgecrest mainshock rupture. Northeast trending faults with sinistral slip shown with red and dextral slip and distributed coseismic strain in blue (taken from Milliner et al., 2021).

https://doi.org/10.5194/egusphere-2026-1948
Preprint. Discussion started: 8 May 2026

2. Methods

For this study we use wet kaolin as the analogue material within the scaled physical experiments that simulate early strike-slip fault development within the upper crustal in the presence of pre-existing weakness with a range of orientations. Wet kaolin produces sharp localized faults and the scaling of clay to crustal strength allows table top experiments to simulate crustal deformation (e.g., Bonini et al., 2016; Elston et al., 2022; Hatem et al., 2015; Henza et al., 2010; Toeneboehn et al., 2018; Bonini et al. 2023). Experiments that last a few hours in the laboratory give us the opportunity to directly observe and document processes that typically span thousands to a million years in the crust. Digital Image Correlation techniques provide spatial and temporal documentation of strike-slip fault evolution not available from field investigations.

2.1 Wet Kaolin Properties

This study uses a wet kaolin clay produced by the pottery industry as #6 tile clay. This kaolin rich material mostly consists of clay and silt particles; approximately 5-10% sand, 30-35% silt, and 60% clay-sized particles (Reber et al., 2020). The high silt content provides low plasticity to the clay which facilitates localized faulting along sharp fault surfaces (Cooke and Van Der Elst, 2012). We use wet kaolin as the analogue material because it produces localized and easy to track faults that are long-lived and because pre-existing weaknesses can be introduced by cutting the clay (e.g., Bonanno et al., 2017; Bonini et al., 2023; Hatem et al., 2017). Prior to failure, wet kaolin deforms as a bi-viscous Burger's material with both elastic and viscous properties that makes it well-suited to simulate inelastic crustal deformation processes at a variety of time scales (Cooke and Van Der Elst, 2012; Elston et al., 2022). At failure, clay exhibits neutral rate and state frictional behaviour that allow faults to creep during experiments (Cooke and Van Der Elst, 2012).

To simulate crustal deformation processes in the laboratory, which is 5 orders of magnitude smaller than the crust, we need to scale the shear strength of the analogue material to be five orders of magnitude weaker than the strength of the crustal material. We adjust the shear strength of the wet kaolin by modifying the water content (Cooke and Van Der Elst, 2012; Eisenstadt and Sims, 2005). In these experiments the kaolin has 70-73% water content by weight to produce 119-123 Pa undrained shear strength with fall cone tests. The density of the wet kaolin used in the experiments discussed here is ~1.6 g/cm^3 (Hatem et al, 2015). We collect samples of wet kaolin before and after each ~2 hours long experiment to assess changes in the water content. The water loss within the upper 1 cm is less than 3% for experiments of this study, which correlates to only ~2 Pa increase in shear strength at the top of the claypack. The bottom half of the claypack does not experience water loss.

The length scaling of the analogue material and the crust follows from the frictional scaling relationship developed by Hubbert (1937) in which the strength ratio of the model to the prototype, or the crust, is equal to the density ratio of the model to the prototype multiplied by the length ratio of the model to the prototype. Using similar coefficients of internal friction for both the analogue material and the Earth's crust (0.55-0.85; Henza et al., 2010; Reber et al., 2020), crustal density of 2.65g/cm^3 and crustal strength of 10-20 MPa, we estimate that 1 cm within the wet kaolin experiment is equivalent to 1-2 km in the Earth's crust. Because the wet kaolin is viscoelastic, in addition to length scaling we also consider the time scales of viscous stress

https://doi.org/10.5194/egusphere-2026-1948
Preprint. Discussion started: 8 May 2026

relaxation in both the experiment and the upper crust. The 15-minute Maxwell relaxation time of the wet kaolin (Cooke and Van Der Elst, 2012) corresponds to 20-200 ka for upper crustal rocks so that one minute in the analogue model simulates 1.3-13 ky in the crust (Elston et al., 2022).

The low but non-zero shear strength of the wet clay has several benefits for the experiments. Fault systems to evolve with both the growth of new faults and persistent slip along favourably oriented faults. Additionally, we can introduce planes of weaknesses into the clay pack by passing an electrified probe through the clay prior to the onset of experiments. The low voltage current neutralizes bonds between clay particles and reduces drag of clay with the moving probe. Because the precut surfaces are weaker than intact clay, these planes may develop slip before development of new faults within the intact clay. Introducing planes of weaknesses into the analogue material provides the opportunity to investigate fault evolution in the presence of existing weaknesses, such as other faults or bedding planes, in the crust (Bonanno et al., 2017; Bonini et al., 2016; Elston et al., 2022; Hatem et al., 2015).

2.2 Experimental Setup

All strike-slip fault experiments use a split box apparatus (claybox) in which one half of the box remains static while a computer-controlled stepper motor applies velocity of 0.5 mm/min to the other half of the box to provide either localized or distributed dextral basal shear (Figure 2). Juxtaposed basal plates create localized basal shear across the velocity discontinuity whereas a 1.5 cm wide elastic TheraBand™ glued to the bottom of the plates creates distributed basal shear. For the distributed basal shear experiments we pre-stretch the elastic shear from 1.5 to 2.5 cm prior to the onset of experiments to reduce undulations that arise when shearing the sheet. A 25 Megapixel DSLR camera with fixed length lens mounted above the experiment captures images at 30 seconds intervals corresponding to ~0.25 mm of applied displacement between images. We emplace the claypack of 2.5 cm thickness into the box from the centre outward to prevent large air bubbles within the clay and scrape the clay to produce a level surface.

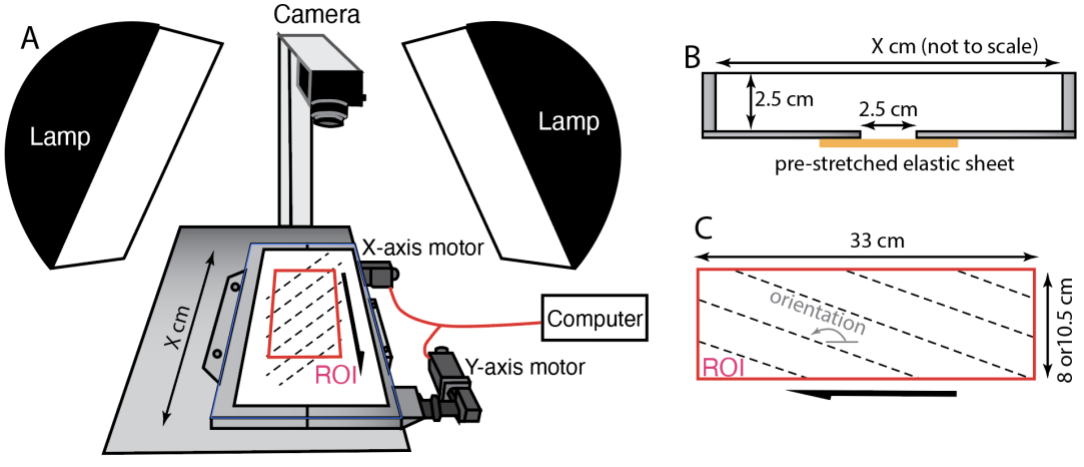

https://doi.org/10.5194/egusphere-2026-1948
Preprint. Discussion started: 8 May 2026

Figure 2. A) Set up for localized basal shear experiments where the plates juxtapose one another. Lamps with diffusers provide even lighting while minimizing glare. B) Cross-sectional sketch of the distributed basal shear experiment that uses elastic sheeting. The region of interest (ROI) was selected to avoid the boundary effects of the claybox apparatus. C) The angle of the precut weakness is counterclockwise from the overall shear direction.

Following the preparation and placement of the clay into the split box apparatus, we utilize a programmable plotter fitted with an electrified probe to introduce vertical weaknesses in the clay with the desired strike orientation and spacing. While the plotter cannot cut surfaces across the entire experiment, the pre-existing weaknesses fill the regions of interest analysed for this study (Figure 2A). After introducing the weaknesses, we sieve red and black sand on the surface of the clay to provide contrasting texture for photos used for Digital Image Correlation, which generates incremental displacement fields from pictures taken throughout the experiment. The average image resolution for the experiments is ~160 pixels/cm.

We vary the initial strike orientation and spacing of the introduced vertical surfaces to assess the impact of different networks of pre-existing weaknesses on strike-slip fault evolution. The suite of experiments includes both localized and distributed basal shear. Experiments without precut weaknesses provide baseline results for comparison. For the localized base shear experiments, we introduce planes of pre-existing weaknesses at initial angles of 60°, 90°, 120°, and 150° measured counterclockwise from the applied dextral shear orientation. We expect that surfaces oriented at 120˚ and 90˚ may develop sinistral slip and surfaces at 150˚ may develop dextral slip (Figure 3). Because the wet kaolin exhibits coulomb failure (Cooke and van der Elst, 2012), the 60˚ surfaces are not expected to slip. The localized basal shear experiments include introduced weaknesses with spacings of both 2 cm and 5 cm. For experiments that include an elastic sheet between the basal plates, we introduce vertical surfaces oriented at 90°, 120°, and 150° with spacing of 2 cm. The results of these experiments can be compared with the results of the 2 cm spacing localized basal shear experiment to assess the impact of distributed loading. The experiments reach total plate displacement of 60 mm with exception of distributed basal shear experiments where the elastic band ripped prior to reaching 60 mm of plate displacement and localized basal shear experiments with 5 cm spacing of introduced surfaces, which were stopped at 30 cm plate displacement to focus on early strike-slip evolution. To assess repeatability, we repeated all the localized basal shear experiments with 2 cm weakness space and several other experimental conditions.

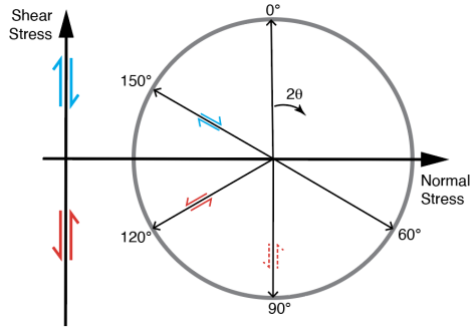

Figure 3. Mohr diagram depicting orientations of pre-cut surfaces used in this study for a general stress state within the shear zone. The maximum shear stress (top of stress state circle) is along the direction of applied shear. The plane orientation, θ, is measured

https://doi.org/10.5194/egusphere-2026-1948
Preprint. Discussion started: 8 May 2026

counterclockwise from the applied shear direction and plotted here as 2θ counterclockwise from the maximum shear direction. Blue indicates dextral shear and red indicates sinistral shear.

2.3 Data processing

We utilize PIVlab 2.63 version for MATLAB (Thielicke and Stamhuis, 2014) to calculate the incremental displacement fields from the time series of overhead photos from each experiment. We select the same region of interest (8 by 33 cm) for analysis for all localized basal shear experiments and an enlarged the width of the region by 2.5 cm for distributed basal shear experiments that include the elastic band (Figure 2c). We adopt the multi-pass PIV workflow from Hatem et al. (2017), which analyses each image pair three times with a descending window size to refine the incremental displacement field to yield data points every 12 pixels. This process results in displacement data every 0.75 mm. From the horizontal displacement field, we calculate the vorticity (two times the curl of the displacement fields) for each stage of the experiment, which reveals the localized strike-slip along faults.

To delineate active faults from the incremental vorticity maps, we use an adaptive threshold filter to detect high strain regions following the approach of Chaipornkaew et al. (2022), Gabriel et al. (2025) and Ramos Sánchez et al. (in review). The adaptive threshold detects faults from the stacked vorticity maps using a sensitivity of 0.1 and a neighbourhood size used to identify zones of localized high shear strain. Smaller or larger neighbourhood sizes impact number of detected faults; larger neighbourhoods pick up noise and small neighbourhoods miss some faults (Ramos Sánchez et al., in review). For our study, we stack five consecutive strain maps to reduce noise and use a neighbourhood size of 5x5 mm^2 to capture small fault details. After applying the adaptive threshold technique to the incremental vorticity maps, we remove additional noise from the active fault maps by eliminating high shear strain regions with fewer than 8 connected pixels (area < 6 mm^2). Additionally, the adaptive threshold technique incorrectly detects faults in some experiments that have noise in low strain regions away from the fault zone. When needed, we filter out these low strain regions by masking the top and bottom ~11 mm of the fault map and only analyse the central region of higher strain. The result of this process is a binary active fault map with the active fault configuration from each stage of each experiment.

We can use the active fault maps to assess the partitioning of strain as slip along faults versus distributed deformation off of faults. For example, the development of slip along the introduced weaknesses may increase off-fault deformation within the strike-slip fault system. To assess off-fault deformation, we estimate the portion of applied velocity that is expressed as incremental slip along the active faults in the direction of the applied loading, called the kinematic efficiency (KE; e.g., Hatem et al., 2017; Gabriel et al., 2025). Kinematically efficient faults have greater fault slip and less off-fault deformation (KE = 1 – off fault deformation). As faults propagate, link, and become throughgoing surfaces, their kinematic efficiency increases (e.g., Cooke et al., 2013; Hatem et al., 2017). Kinematic efficiency estimates only use the component of fault slip measured in the same direction as the applied velocity because we are interested in how the applied strain is partitioned on and off of faults. More efficient strike-slip fault systems that accommodate greater slip also tend to have lesser fault roughness and narrower fault zone width. In order to measure the width of the primary shear zone, we follow the method used by Hatem et al. (2017)

https://doi.org/10.5194/egusphere-2026-1948
Preprint. Discussion started: 8 May 2026

and measure the width of the central zone that accommodates 60% of the applied shear. Along each transect across the fault network, we measured the distance between where the incremental displacement at the surface of the clay reaches 20% and 80% of the applied basal plate displacement. This measurement includes both the fault core and the nearby off-fault deformation. We average the shear zone width and calculate the standard deviation from 446 transects across the fault.

3 Results

All experiments with different basal boundary conditions, pre-existing weakness orientations, and spacings show the three stages of strike-slip fault evolution defined by Hatem et al. (2017) for experiments without pre-existing weaknesses. Prior to the emergence of any faults, the experiments show distributed shear that later localizes along right-stepping echelon faults during stage 1 (Figure 4a). These echelon faults develop over the basal and lengthen by propagation during stage 1. During stage the active fault network reorganizes through propagation, abandonment, and linkage of the echelon faults (Stage 2; Figure 4b); the onset of reorganization is marked with thinning of the shear zone as outboard fault segment are abandoned. With further deformation the faults formed a continuous fault surface (Stage 3; Figure 4c). The timing, and duration of these stages varied for different experimental conditions (Figure 5). Some of the experiments with introduced weak surfaces also show an early phase of activation of slip along those surfaces prior to the development of new echelon faults. Here we consider stage 1 to start when slip localizes along faults, either along new faults or along introduced weaknesses. In addition to analysing the activation of the pre-cut surfaces and impact of these surfaces on fault network evolution, we analyse the evolution of both kinematic efficiency of the fault system and the overall shear zone width.

The activation of slip along pre-existing weakness occurred in experiments with surfaces at some but not all orientations; the relationship of orientation and activation was similar for experiments with different basal shear and spacing of pre-existing weaknesses. We first describe the results from the localized basal shear experiments with 2 cm spacing of precut surfaces and then highlight fault system evolution differences for the experiments with distributed basal shear and 5 cm spacing between precut surfaces. For all suites of experiments, the results from the uncut experiments serve as a benchmark to assess the impact of pre-existing weaknesses on strike-slip fault system evolution.

3.1 Impact of weakness orientation over localized basal shear with 2 cm spacing

Localized basal shear experiments with 2 cm spacing of pre-existing weaknesses oriented at 60˚ or 90˚ from the applied dextral shear direction did not show evidence of early slip along the introduced surfaces in any of the experiments (Figure 4d and g). Instead, shear strain localized along new right-stepping echelon faults and the active fault network initiated similarly to the experiment with no pre-existing weaknesses (Figure 4a-b, 4d-e, 4g-h). The new echelon faults had similar spacing and orientation as in the uncut experiment. During stage 1 of the 60˚ and 90˚ experiments, many of the early echelon faults terminate at precut surfaces (red circles on Figure 4h). The precut surfaces in the 90˚ experiment have stronger control on echelon fault terminations than in the 60˚ experiment where many early faults develop across the precut surfaces. Even though the precut

https://doi.org/10.5194/egusphere-2026-1948
Preprint. Discussion started: 8 May 2026

surfaces did not slip early in the experiments, they impacted the development of the early faults in both the 60˚ and 90˚ experiments. All three localized basal shear experiments with no slip along pre-existing weaknesses (i.e., uncut, 60°, and 90°) required similar amount of plate displacement to reach the first two stages of strike-slip fault evolution (Figure 5). The experiment with 90˚ experiments required ~12 mm greater displacement to create a continuous strike-slip fault than the uncut and 60˚ experiments. (Figure 5). The delay in developing a through-going fault surfaces may be due to the strong segmentation of early faults that terminated at many precut surfaces in the 90˚ experiment; more irregular initial fault geometry may require greater strain to develop a connected fault surface.

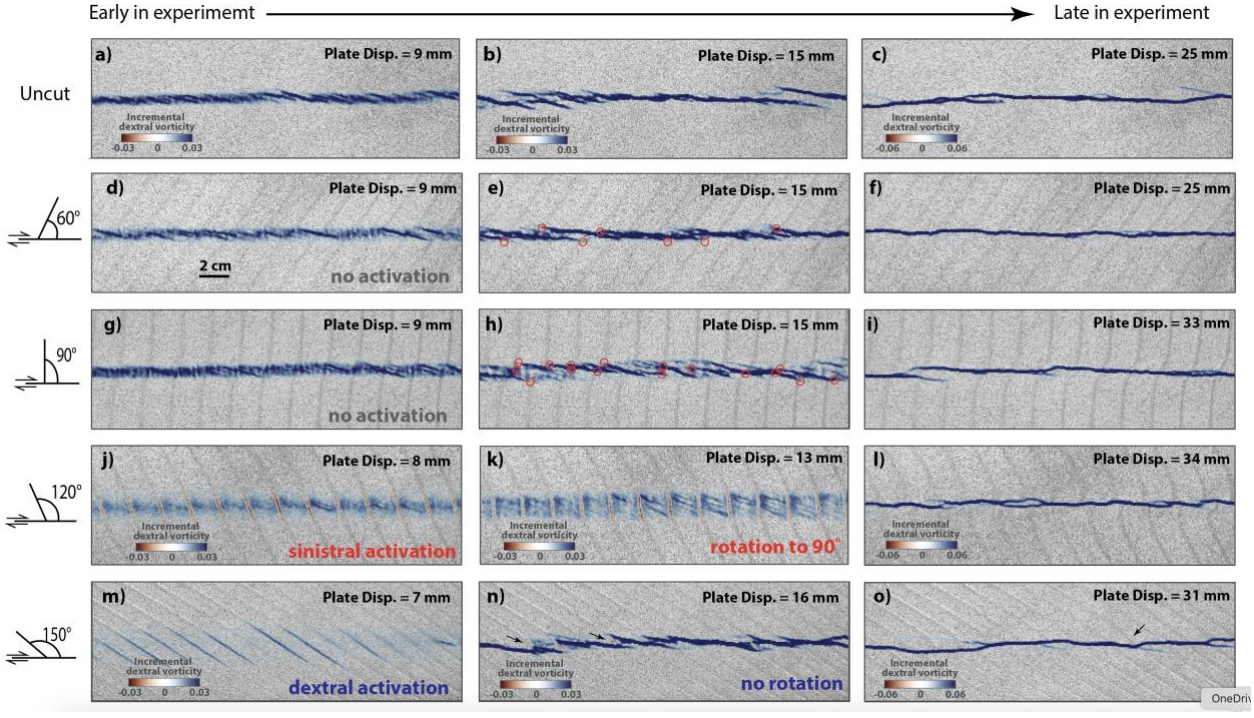

Figure 4. Incremental vorticity maps for localized basal shear experiments with (a-c) no pre-existing weaknesess, (d-f) with 2 cm spaced pre-cut surfaces oriented 60° from the applied shear, (g-i) 90°, (j-l) 120°, and (m-o) 150°. The incremental vorticity color scale for the late in experiment strain maps (right column) is double that of the other stages. (d-i) Experiments with pre-cut surfaces initially oriented 60° and 90° showed no activation of the pre-existing weaknessess. Red circles on highlight where early echelon faults terminated at 60˚ and 90˚ precut surfaces. (j-l) Pre-existing planes of weaknessess oriented 120° from the applied shear exhibited early sinitral slip and distributed dextral shear that produces shear zone rotation. (m-o) Pre-cut surfaces oriented 150° from the applied shear exhibited early dextral slip with no rotation within the shear zone. Arrows point to segments of precut surface that have sinistral slip.

https://doi.org/10.5194/egusphere-2026-1948
Preprint. Discussion started: 8 May 2026

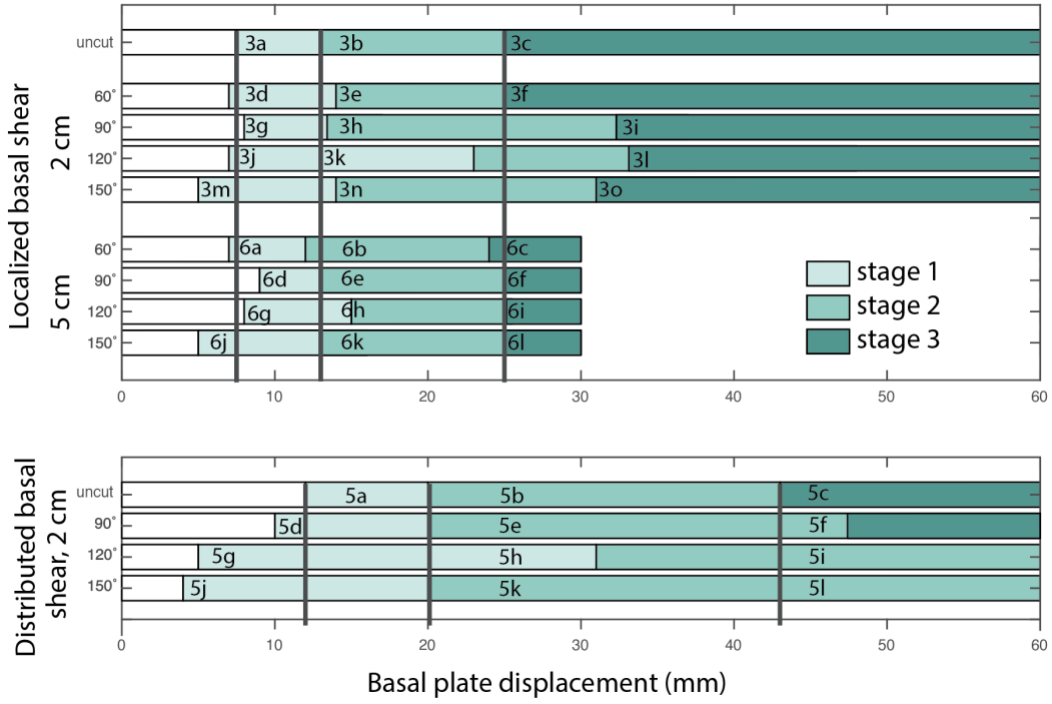

Figure 5: Timing of the onset of stage 1 (emergence of early faults), stage 2 (reorganization of the active fault system) and stage 3 (continuous active fault surface) for experiments with different basal shear conditions and spacing between pre-cut weaknesses. The horizontal position of the number-letter text indicates the plate displacement of that image.

The localized basal shear experiments with 2 cm spaced weaknesses oriented 120° from the applied shear developed sinistral slip along the weaknesses early in the experiment (Figure 4j). This slip developed with similar plate displacement as the emergence of new echelon faults in the uncut experiment (Figure 5). The distributed dextral shear between the slipping surfaces creates clockwise rotation within the fault zone (Figure 4j-k). Consequently, sinistral faults that started oriented 120˚ from the direction of primary shear rotated clockwise and continued to show sinistral slip until they were oriented just beyond 90° from the applied shear direction (Figure 4j-k). With this decrease in sinistral slip along the pre-existing weaknesses, shear strain localized onto new dextral echelon faults located in between the precut surfaces marking the start of Stage 2 (Figure 4k). During stage 2, these new echelon faults propagated across the pre-cut surfaces and linked without any further slip along the pre-cut surfaces. The onset of stages 2 and 3 in the experiment with 120˚ weaknesses occurred with greater basal plate displacement than for the uncut experiment (Figure 5). The highly segmented geometry of initial faults required great strain for through-going fault development.

The experiments with weaknesses oriented 150˚ from the applied shear direction developed early dextral slip (Figure 4m). The activation of dextral slip occurred at lower cumulative plate displacement than the emergence of echelon faults in the uncut experiment (Figure 5). The experiments with pre-cut faults oriented 150˚ did not have early distributed shear between the slipping surface and did not show significant rotation within the shear zone, such as documented in the 120˚ pre-cut surfaces

https://doi.org/10.5194/egusphere-2026-1948
Preprint. Discussion started: 8 May 2026

experiments. After dextral reactivation of the 150° pre-cut surfaces, new dextral echelon faults with orientation closer to that of the applied shear (~165˚) developed between the pre-cut surfaces (Figure 4n). The 150˚ faults became inactive as the new echelon faults propagated across the precut surfaces. This reorganization of the active faults system marks the stage of stage 2, which occurred at similar cumulative plate displacement as for the uncut experiment (Figure 5). During stages 2 and 3 the 150˚ experiment developed a few small segments of sinistral slip along the weaknesses between and adjacent to the dextral faults (arrows in Figure 4n and o). Within additional applied strain, the faults within experiment with 150˚ orientated weaknesses formed a throughgoing surface with remnant irregularities from the pre-existing weaknesses (Figure 4o). The onset of stage 3 in this experiment required greater cumulative plate displacement than for the uncut experiment (Figure 5). As with the 90˚ and 120˚ experiments, the irregularity of the initial faults required greater strain for the development of a continuous fault surface.

3.2 Impact of distributed basal shear

The experiments with distributed basal shear produced similar fault evolution, precut weakness activation and fault zone rotation as the localized basal shear experiments but required greater plate displacement to reach each stage of strike-slip fault evolution (Figure 5). For example, distributed basal shear experiments with 120˚ and 150˚ weaknesses did not develop a through-going fault surface by the end of the experiment with 60 mm of basal plate displacement (Figure 4.) For experiments with no slip along precut surfaces (i.e., uncut and 90˚) distributed basal shear produces longer echelon faults than localized basal shear (Figure 6 b&e versus Figure 4 b&h). These longer echelon faults lead to wider step overs and a more rough and segmented fault surfaces late in the distributed basal shear experiments (Figure 4c & f). The distributed nature of basal shear produced local rotation of material within the wide shear zone (Figure 4e). The earliest echelon faults in the 90˚ experiment terminate at precut surface (stage 1; Figure 4d); later during stage 2 the faults pattern was less impacted by the position of the precut surfaces (Figure 4e). When the sinistral faults of the 120˚ experiment rotated to 90˚, some new small sinistral faults developed between the precut surfaces (Figure 4h). The two experiments where pre-cut surfaces slipped (120° and 150°) develop long and widely spaced echelon faults in Stage 2 that crosscut the precut surfaces (Figure 6i&k). The 150˚ experiment showed sinistral slip along sections of the pre-existing weaknesses between active dextral fault segments (Figure 6k). For the experiment with 150˚ weaknesses, the wide zone of faulting leads to the development of multiple parallel faults none of which are continuous across the region of interest by the end of the experiment (Figure 6l).

https://doi.org/10.5194/egusphere-2026-1948
Preprint. Discussion started: 8 May 2026

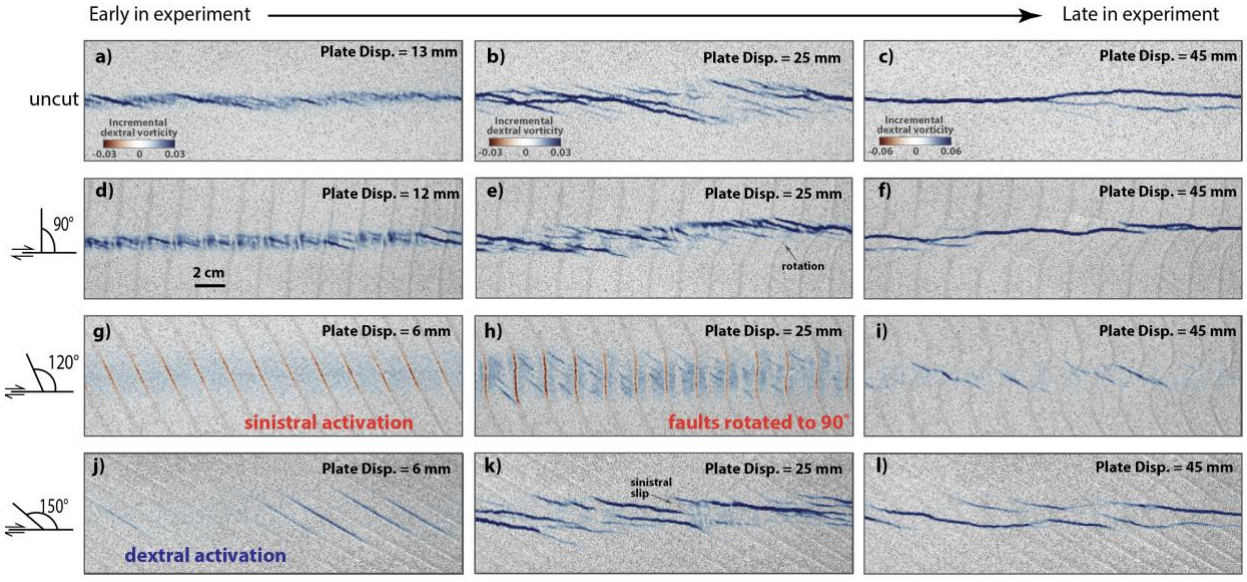

Figure 6. Incremental vorticity maps for distributed basal shear experiments with (a-c) no pre-cut surfaces, with 2 cm spaced pre-cut surfaces oriented (d-f) 90°, (g-i) 120°, and (j-l) 150°. (d-f) The incremental vorticity color scale for the late in experiment strain maps (right column) is double that of the other stages. Experiments with pre-existing surfaces initially oriented at 90° showed no activation of the pre-existing weaknesses. (g-i) Pre-existing planes of weaknesses oriented 120° from the applied shear exhibited sinitral slip and distributed dextra shear that produced clock-wise rotation within the shear zone. (j-l) Pre-cut surfaces oriented 150° from the applied shear exhibited early dextral slip with no shear zone rotation.

3.3 Impact of weakness spacing

Localized basal shear experiments with 5 cm wide pre-cut surfaces showed similar strike-slip fault evolution as the localized basal shear experiments with 2 cm pre-cut surfaces (Figures 4 & 7). Despite introducing wider spaced pre-cut surfaces into the wet kaolin, the experiments did not need greater plate displacement than the closely spaced pre-cut surface experiments to reach stages 1 and 2 of strike-slip fault evolution (Figure 5). In fact, the early echelon faults within experiments with 90˚ precut surfaces of 5 cm spacing started reorganizing (stage 2) with lesser plate displacement than for those with 2 cm spacing (Figure 5). Unlike the experiment with 2 cm spacing, the termination of early echelon faults in 90˚ experiment with 5 cm spacing precut surfaces are not strongly controlled by the position of the surfaces (Figures 4h & 7e). The experiments with precut surfaces at 120˚ and 150˚ that showed early slip had similar strain required for early activation, shear zone rotation (if present), abandonment of slip along the pre-cut surfaces, and localization of strain onto new echelon faults located in between the surfaces. The wider spacing of the weaknesses allow for growth of longer new echelon faults than in the 2 cm spacing experiments (Figure 7 h&k vs Figure 4 k&n). Interestingly, the experiments with wider spaced 120˚ and 150˚precut surfaces developed continuous fault surfaces with lesser displacement than the experiments with 2 cm spaced weaknesses (Figure 5). Furthermore, irregularities along the through-going fault of the widely spaced pre-cut experiments (Figure 7f, i & l) have farther spacing than the irregularities of equivalent closely spaced pre-cut experiments (Figure 4l and o). These observations are consistent with pre-existing weaknesses controlling the development of long-lasting fault irregularities.

https://doi.org/10.5194/egusphere-2026-1948
Preprint. Discussion started: 8 May 2026

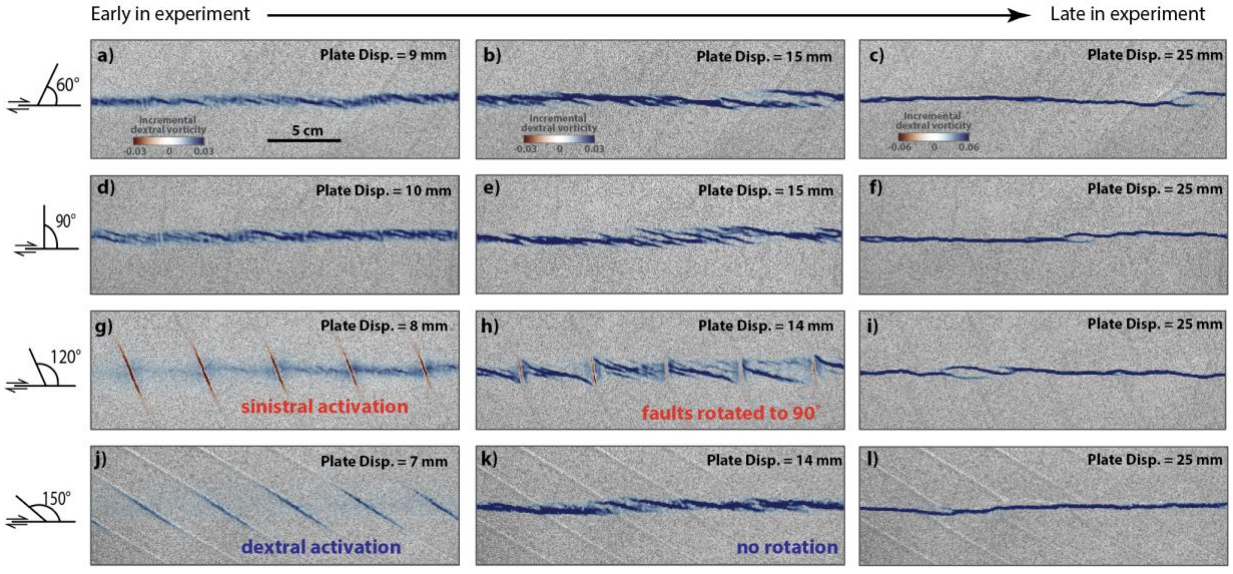

Figure 7. Incremental vorticity maps for localized basal shear experiments with widely spaced (5 cm) pre-cut surfaces oriented (a-c) 60° from the applied shear, (d-f) 90°, (g-i) 120°, and (j-l) 150°. The incremental vorticity color scale for the late in experiment strain maps (right column) is double that of the other stages. (a-f) Experiments with pre-cut surfaces initially oriented between 60°and 90° showed no activation of pre-existing weaknessess. (g-i) Pre-existing planes of weaknessess oriented 120° from the applied shear exhibited strong sinitral slip and clock-wise rotation. (j-l) Pre-cut surfaces oriented 150° from the applied shear exhibited dextral slip with no rotation.

3.4 Partitioning of strain as pre-existing weaknesses evolve:

In order to assess the impact of pre-existing weaknesses on the partitioning of shear strain as localized fault slip and distributed off-fault deformation, we track the evolving kinematic efficiency of the evolving fault systems. (Figure 8). All experiments began with 0% kinematic efficiency as the applied loading was accommodated as off-fault deformation and kinematic efficiency increased as the faults evolved and accommodated greater slip. Because the experiments with different precut surface spacing and basal loading evolve similarly, we limit detailed analysis here to the evolving kinematic efficiency of experiments with localized basal shear and 2 cm spacing between pre-cut surfaces.

https://doi.org/10.5194/egusphere-2026-1948
Preprint. Discussion started: 8 May 2026

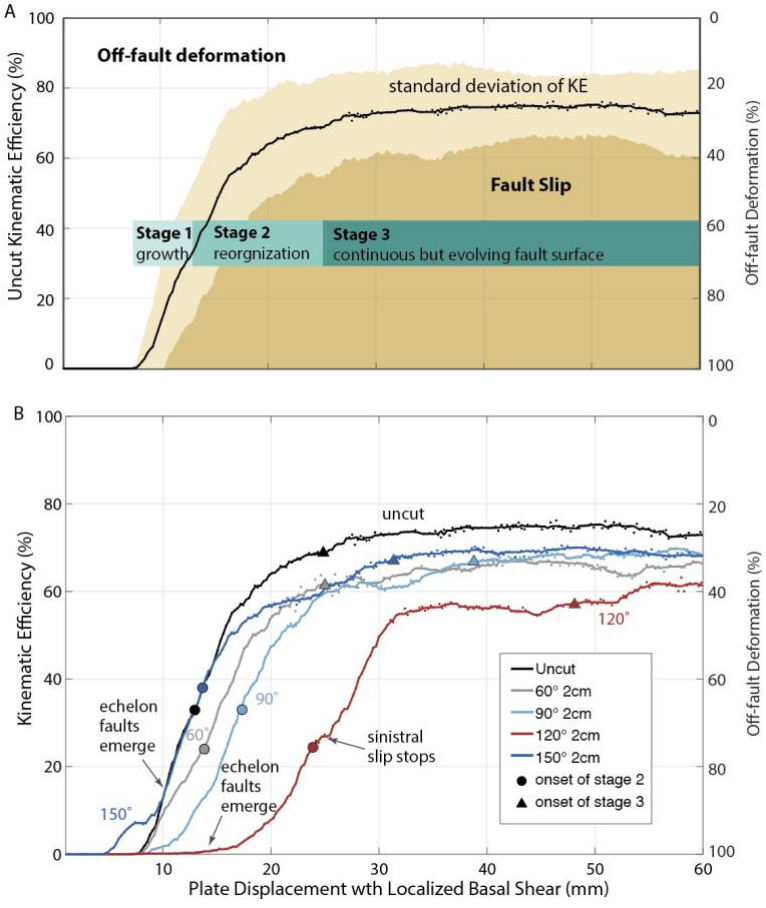

Figure 8. A) Kinematic efficiency and off-fault deformation versus plate displacement for uncut experiment with localized basal shear. The line is a 5-point median filter through the data with standard deviation in light grey. The uncut experiment serves as a baseline for assessing the impact of the pre-existing weaknesses on strike-slip fault evolution. B) Kinematic efficiency and off-fault deformation versus plate displacement for all localized basal shear experiments with 2 cm spacing between pre-cut surfaces. The symbols indicate onset of the stages 2 and 3 of strike-slip fault evolution. Stage 1, the early localization of shear along existing weaknesses or new echelon faults, starts when KE>0. Stage 2 shows continued localization of strain as fault slip as echelon faults reorganize by propagation, abandonment, and linkage. By Stage 3 the experiments have formed continuous fault surface.

The evolution of kinematic efficiency for the uncut experiment serves as a baseline for assessing the impact of pre-cut surfaces on fault evolution. The kinematic efficiency started increasing in the uncut experiment with the emergence of the first right-stepping echelon faults at around 8 mm of plate displacement (start of stage 1; Figure8a). The slip along the echelon faults increased as they propagated in stage 1 and as they reorganized during stage 2, which started ~13 mm plate displacement. At around 25 mm of plate displacement, the fault developed a throughgoing surface (onset of stage 3; Figure 8a) and the kinematic efficiency for the uncut localized experiment approached 70%, which indicates that 30% of applied deformation was distributed as off-fault deformation. As the fault continued to slip and change its active trace, the kinematic efficiency approached 75% (25% off-fault deformation) and remained around that value for the rest of the experiment (Figure 8a). This steady-state kinematic efficiency is lower that values reported for similar experimental conditions by Hatem et al. (2017),

https://doi.org/10.5194/egusphere-2026-1948
Preprint. Discussion started: 8 May 2026

which reached 90% kinematic efficiency. Hatem et al. (2017) used a global incremental strain threshold to detect faults, which differs from the adaptive threshold used here; differences in fault detection method change the estimates of off-fault deformation (Ramos Sánchez et al., in review). For the purposes of this study, we are interested in how the kinematic efficiency (and off-fault deformation) changes between experiments rather than the specific values of the efficiency.

The uncut experiment has the highest kinematic efficiency of all experiments, indicating that even when pre-cut surfaces oriented at 60˚ and 90˚ did not show slip at the start of the experiment, these pre-existing weaknesses contributed to of off-fault deformation (Figure 8b). The segmentation of early faults in the 60˚ and 90˚ experiment due to the pre-existing surfaces (Figure 4) also reduces kinematic efficiency during stage 1. While the 90˚ experiment required greater strain to develop a through-going fault surface, its kinematic efficiency at the onset of stage 3, 66%, is similar to that of the uncut and 60˚ experiments, 68% and 63% respectively (Figure 8b). The steady-state kinematic efficiency of the experiment with 90˚ weaknesses during stage 3 is similar to that of the 60˚ weakness experiments, indicating similar partitioning of strain on and off of the faults once the continuous surface developed. For these experiments without early slip along pre-cut surfaces, 30-35% of the deformation is accommodated off of the mature through-going fault (Figure 8b).

The experiment with pre-cut surfaces oriented 120° from the applied shear direction had much lower kinematic efficiency than the other experiments. The 120° pre-cut surfaces experienced sinistral slip at around 8 mm of plate displacement but because of the orientation of this slip and the low slip rates, the component of overall right-lateral slip parallel to the loading direction detected with the kinematic efficiency remained near zero until after 10 mm of plate displacement (Figure 8b). For much of stage 1 dextral strain of the fault system was accommodated by distributed off-fault strain between the sinistrally slipping weaknesses, leading to low kinematic efficiency. By 13 mm of plate displacement slip along the pre-cut surfaces decreased and strain started to localize on new right-stepping echelon faults, which the increased kinematic efficiency of the active fault network. Even after the 120˚ experiment developed a continuous slip surface in stage 3, the off-fault deformation remains higher (~40%) than all other experiments (Figure 7).

The experiment with 150° pre-cut surfaces showed the earliest localization of slip at ~5 mm of plate displacement; dextral slip along the favourably oriented pre-existing weaknesses increased the kinematic efficiency of the system. With further plate displacement, the emergence of new echelon faults that formed between the pre-cut surfaces around 10 mm of plate displacement increased kinematic efficiency to 15% (Figure 8b). During the subsequent reorganization of the fault network in stage 2 the kinematic efficiency reached almost 40%. With continued plate displacement, the experiment generated a continuous slip surface after 30 mm of plate displacement with a kinematic efficiency of ~68% during stage 3. The kinematic efficiency values for the mature fault system in the 150˚ experiment are similar to those of the 60° and 90° pre-cut surface experiments with about 30-35% off-fault deformation (Figure 8b).

https://doi.org/10.5194/egusphere-2026-1948
Preprint. Discussion started: 8 May 2026

3.5 Evolution of shear zone width:

We analysed the average width of the shear zone that accommodates 60% of the total shear strain for all localized basal shear experiments with closely spaced (2 cm) pre-cut surfaces. The results for the uncut experiment and its standard deviation serve as a baseline for assessing the impact of pre-existing weakness on the evolution of the shear zone width (Figure 9).

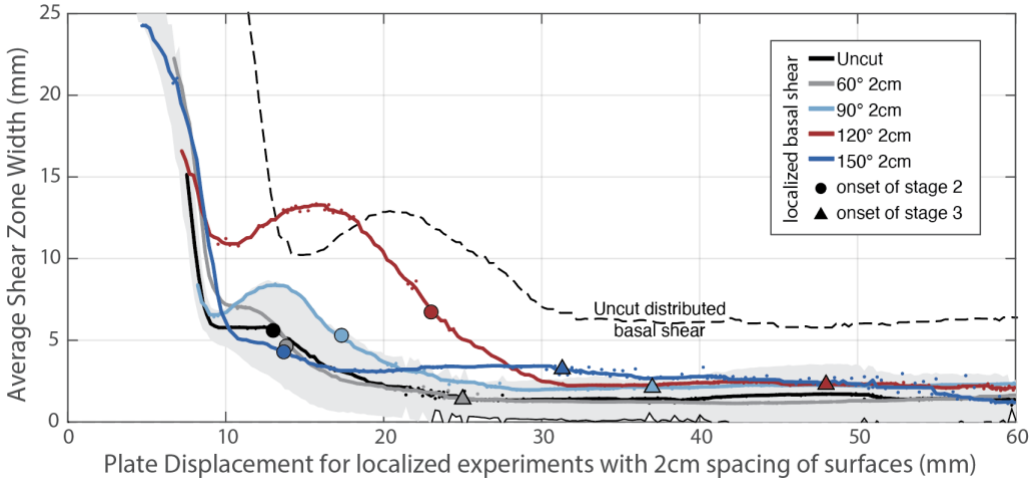

Figure 9. Evolution of shear zone width for experiments with localized basal shear and 2 cm spacing of precut surfaces after the emergence of faults (start of stage 1. The lines are 5-point median filter through the data points. The grey region shows the standard deviation for the uncut experiment, which serves as a baseline for the experiments with 2 cm spaced pre-cut surfaces oriented 60°, 90°, 120°, and 150° from the applied dextral shear. The symbols indicate the onset of different stages of strain localization as strike-slip fault evolve. The width of the mature faults are similar to each other, suggesting that mature fault zone width may not reveal the role of early weaknesses on fault evolution.

All of the experiments started with wide zones of distributed deformation that during the evolution of the strike-slip faults narrow nonlinearly with accumulated plate displacement (Figure 9). In the uncut experiment, the shear zone width decreased after the emergence of the first faults (onset of stage 1 Figure 9). As the new echelon faults developed, the shear zone remained about 6 mm wide. Around 15 mm plate displacement, the early echelon faults started to propagate and reorganize (onset of stage 2) and the shear zone width decreased until reaching a width of around 1.4 mm at the later stages of fault evolution (Figure 9).

Experiments with surfaces oriented 60° and 90° from the applied shear direction showed similar shear zone width evolution to the experiment with no pre-existing weaknesses and plot within the standard deviation of the uncut experiment. The shear zone width decreased after the earliest faults emerged at until ~10 mm of plate displacement for both experiments, after which the width remained ~7 mm wide for the 60° pre-cut surfaces experiment while the 90° experiment experienced a small increase in width to 8 mm. At ~15 mm of plate displacement, the echelon faults interacted with the 90˚ pre-cut, which contributed to a wider average shear zone width compared to the 60° and uncut experiments (Figure 9). During stage 2, the reorganization of echelon faults decreased the average shear zone width in both the 60˚ and 90˚ experiments and with the development of a continuous slip surface, stage 3, the mature faults have similar shear zone width to the uncut experiment.

https://doi.org/10.5194/egusphere-2026-1948
Preprint. Discussion started: 8 May 2026

The experiment with 120° pre-cut surfaces produced the widest shear zone during stage 1 of early fault activation and growth when the cross-faults were active. The initial decrease in shear zone width upon the localization of sinistral slip along the pre-cut surfaces was followed by an increase in shear zone width at ~11 mm of plate displacement. While increases in shear zone width are typically associated with echelon fault growth, here the width increase is due to rotation of the fault segments within the shear zone to ~90° from the applied shear direction (Figure 4k; Figure 9). After the pre-cut surfaces became inactive at ~17 mm of plate displacement and new echelon faults emerged between the pre-cut surfaces, the shear zone width decreased. During stage 2. the shear zone width continued to thin as the echelon faults propagated, linked, and reorganized. The mature shear zone during stage 3 had similar width to the uncut experiments (Figure 9).

The average shear zone width for the experiment with 150° pre-cut surfaces evolves similarly to the uncut experiment with a few differences. Around 10-15 mm plate displacement (near end of stage 1) the 150˚ experiment has narrower shear zone that the uncut experiment because the early slip along the favourably oriented pre-cut surfaces jumpstarted the strike-slip fault evolution (Figure 9). In stage 2, the fault system reorganized to form new echelon faults with shallower orientation than the pre-cut surfaces and the fault network that had both early and new faults produced wider shear zone than the uncut experiment (Figure 9). In stage 3, the mature fault in the 150° pre-cut experiment has a similar fault shear zone width (~2 mm) to the uncut experiment (Figure 9).

The experiments with distributed basal shear generally have wider shear zones than the experiments with localized basal shear, consistent with the experimental results of Hatem et al. (2015). For ease of presentation, we only show shear zone evolution of the distributed basal shear uncut experiment on Figure 9 with the localized shear results.

4. Discussion

The angle of pre-existing weaknesses with respect to the overall shear direction strongly impacts the development of early strike-slip faults, regardless of spacing of the weaknesses and whether basal shear is distributed or localized. Early segmentation of strike-slip faults leaves fingerprints in the irregularly geometry of the mature through-going faults.

4.1 Repeatability of fault evolution

To confirm the observations documented throughout each experiment, we repeated many experiments with the same laboratory and material conditions (Table 1). We confirm that the findings presented in section 3 persist for each localized basal shear experiment with closely spaced pre-cut surfaces. Experiments with 60° and 90° pre-cut surfaces did not show early slip along the weaknesses and the 90˚ experiment had greater degree of early echelon faults terminating at precut surface than the 60˚ experiment. Within the 120° experiments, the pre-cut surfaces reactivated with sinistral slip and the early distributed dextral shear rotated the slipping surfaces to 90° from the applied shear. Within the experiments with 150˚ pre-cut surfaces the surface activated with dextral slip but did not rotate.

https://doi.org/10.5194/egusphere-2026-1948
Preprint. Discussion started: 8 May 2026

Experiment	Basal Shear	Spacing of pre-cut surfaces	Angle of surfaces	Final Displacement
08_21_23a	Localized	5 cm	90°	30 mm
08_21_23b*	Localized	2 cm	90°	30 mm
08_22_23a	Localized	5 cm	60°	30 mm
08_22_23b*	Localized	2 cm	60°	30 mm
08_23_23a	Localized	5 cm	120°	30 mm
08_23_23b*	Localized	2 cm	120°	30 mm
08_24_23a	Localized	5 cm	150°	30 mm
08_24_23b*	Localized	2 cm	150°	30 mm
08_29_23a*	Localized	5 cm	120°	60 mm
08_29_23b	Localized	2 cm	120°	60 mm
09_05_23b	Localized	2 cm	90°	60 mm
09_06_23b	Localized	2 cm	150°	60 mm
10_08_23b	Localized	2 cm	60°	60 mm
10_10_23b*	Localized	2 cm	60°	60 mm
09_07_23	Localized	none	-	60 mm
09_13_23b	Distributed	2 cm	90°	60 mm
09_14_23b	Distributed	2 cm	120°	60 mm
09_21_23b	Distributed	2 cm	150°	60 mm
10_09_23	Distributed	none	-	60 mm

Table 1: Listing of all experiments. Results of experiments noted with * have repeated conditions to assess repeatability and results are not presented in the main text.

4.2 What does slip along pre-existing weaknesses tell us about material and fault strength?

Plotting stress states on a Mohr diagram (Figure 10a) provides a way to visually represent potential slip envelopes for 1) the initiation of slip along pre-cut surfaces (solid line) and 2) the continued slip along surfaces with some degree of slip weakening (dashed line).

Pre-cut surfaces oriented 60˚ and 90° to the applied shear direction have no early activation and fall below the envelope for slip along pre-cut surfaces. Figure 10a shows that weaknesses within the shear zone oriented at 30˚ (not tested in the experiments) are not expected to slip because their stress state is far from the slip threshold. Consequently, we expect that any weak surfaces oriented ~30°to ~90° or ~210˚ to ~270˚ from the primary shear direction may not show early slip (grey regions on Figure 10b).

On the other hand, pre-cut surfaces at 120° from the applied shear direction showed prominent early sinistral slip implying that the stress state along these surfaces is at (or exceeding) the threshold for sinistral slip (Figure 10a). Pre-existing surfaces at 150° from the applied shear showed dextral slip indicating that the stress state meets (or exceeds) the threshold for slip along these surfaces (Figure 10a). Because the primary fault is oriented 0˚ (and 180˚), this orientation will show early dextral slip.

https://doi.org/10.5194/egusphere-2026-1948
Preprint. Discussion started: 8 May 2026

From these results we expect that weaknesses within shear zones oriented in the blue and red regions of Figure 10b would have dextral and sinistral slip, respectively. Figure 10a also shows that the stress states along weaknesses oriented 135˚ degrees, midway between 120˚ and 150˚, would not likely slip because the stress state does not reach the frictional slip threshold.

The experimental results show that while pre-cut surfaces oriented at 90˚ to the applied shear direction did not slip, pre-cut surfaces oriented 120° from the applied shear that slipped and rotated to 90˚ did exhibit small sinistral slip (dashed arrows on Figure 10a). This observation suggests that the slip threshold for surfaces that have previously slipped, and consequently experienced slip weakening is lower than the threshold to initiate slip (Figure 10a). The process of accruing slip along the surfaces may align the clay particles and/or draw water to the fault zones that reduces its strength. By mapping the observations from the different experiments into the Mohr diagram, the claybox acts like an experimental rheometer to inform the properties of the clay.

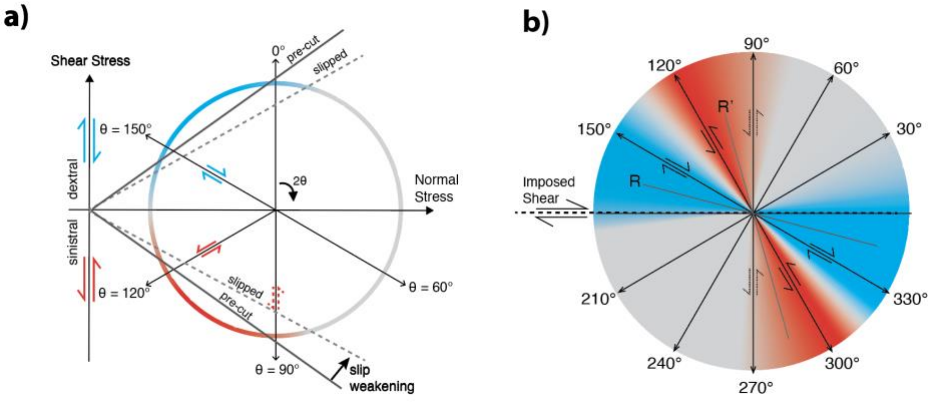

Figure 10. a) Schematic Mohr diagram depicting hypothetical stress state within the shear zone with orientation of pre-cut surfaces used in our study. Dextral shear is positive. Colour of the arrows indicate the sense of slip and dotted arrows indicate small amounts of slip. Envelopes show stress conditions for initial slip along the pre-cut surfaces (solid) and for surfaces that have previously slipped (dashed). b) Diagram of real-world orientations for the pre-cut surfaces with expected sense of slip. R and R' indicate Riedel shear naming system used by many researchers (Davis et al., 2000).

The array of early faults formed by early slip along weaknesses can be described using Riedel shear nomenclature used by many previous researchers of fault zone structures (Davis et al., 2000). Surfaces at low angles to the shear zone that have slip consistent with the shear zone are called R shears and surfaces at higher angles to the shear zone that have slip opposite to the primary shear zone are called R' shears. While the Riedel terminology is efficient for experts to describe fault patterns, we find that this difficult to learn terminology impedes wider understanding and sometimes leads to misinterpretation of slip from fault patterns. For these reasons, we prefer to describe the geometry and slip sense along the early arrays rather than use the R and R' shorthand. In crustal fault studies, the array of short faults at high angle to and having opposing slip to the shear zone (R' shears) are sometimes called cross-faults. This term is more easily understood by non-experts than the Reidel terminology.

https://doi.org/10.5194/egusphere-2026-1948
Preprint. Discussion started: 8 May 2026

4.3 What do strike-slip fault experiments with pre-existing weaknesses tell us about the faults that hosted the Ridgecrest ruptures?

The northwest section of the Ridgecrest mainshock rupture is characterized by a series of secondary parallel, NE-trending sinistral faults that are orthogonal to the primary NW-trending dextral faults (Figure 1b). This series of cross-faults are believed to predate the 2019 rupture and were re-activated during the Ridgecrest event (Antoine et al., 2021). Several mechanisms have been proposed for the sinistral slip along these small cross-faults. Milliner et al. (2021) proposed that the NE trending faults slip sinistrally in response to rotation of individual blocks inside the dextral shear zone; this follows a 'bookshelf' faulting pattern (e.g., Freund, 1974) proposed for many regions including eastern California (e.g., Luyendyk et al., 1980; Platt and Becker, 2013). Antoine et al, (2021) propose that sinistral slip might be fingerprints of the rupture process as the stresses near the propagating rupture tip triggered slip along these pre-existing structures. These proposed mechanisms are not exclusive of one another as the same stress state can arise by multiple mechanisms.

The experiments with weaknesses oriented 120˚ from the applied shear show localized sinistral slip along cross faults as well as distributed dextral shear that produces rotation within the shear zone that resemble the pattern at the northwest section of the Ridgecrest mainshock, which is also consistent with the bookshelf faulting kinematic model. This kinematic model describes active strain portioning of localized slip and distributed shear but does not inform the evolution of these faults. The experiments of this study demonstrate that localized faulting and distributed shear that yields rotation develop simultaneously (Figures 4j, 5g, 6g) and continue until the cross faults are no longer active. One distinction between the experiments and the bookshelf model is that the distributed strain between experimental cross-faults does not yield uniform displacement implied by the rigidity of the 'books' of the bookshelf model. Because the centre portion of the cross-faults experiences greater rotation than the distal portions, the experimental faults of this study develop a sigmoidal shape, similar both to that of previous experiments (e.g., Schreurs, 1994) and to the cross-faults of the northwestern portion of the Ridgecrest mainshock rupture (Figure 1; Antoine et al., 2021). While the faults within the experiments creep and do not express dynamic rupture tip stresses that might contribute curved cross-faults (Okubo et al., 2019), the experimental results suggest that distributed rotation can produce curved faults with or without dynamic stress contributions.

The experimental strike-slip fault evolution suggests that pre-existing cross-faults might become inactive in the future as dextral strain within the fault zone both continues to rotate the cross-faults and localizes along new right-stepping dextral fault segments. With continued deformation the new fault segments might propagate and link to create a mature throughgoing dextral strike-slip fault surface with remnant irregularities from the pre-existing structures.

Our discussion thus far has been on the small sinistral faults along the northwestern part of the Ridgecrest main rupture; however, the M7.1 rupture was preceded by a M 6.4 foreshock along a NE-SW trending sinistral fault with similar NE-SW trend as the sinistral faults along the northwestern part of the Ridgecrest main rupture (e.g., Ponti et al., 2020). Fialko and Jin (2021) point out weaknesses of various mechanisms, including deep ductile flow, low friction and dynamic stresses, proposed for the production simultaneously active orthogonal faults. They use geodetic data to show that regional strain could have rotated sinistral faults that formed in more optimal orientation to their current cross-fault orientation (Fialko and Jin, 2021).

https://doi.org/10.5194/egusphere-2026-1948
Preprint. Discussion started: 8 May 2026

Under conditions of regional simple shear, such as the experiments of this study, the dextral faults do not rotate but the sinistral faults will rotate (e.g., Platt and Becker, 2013) until their orientation and strength do not allow for continued slip. The experimental results suggest that both small and large cross-faults in the Ridgecrest area may be near the end of their activity as new dextral fault segments develop across the sinistral cross-faults. As these dextral faults link up, their increased length and slip will reduce off-fault deformation and increase seismic hazard from future earthquakes.

5. Conclusion

Our study reveals that the presence of pre-existing weaknesses impacts the amount of off-fault deformation even if the weaknesses do not slip. Pre-existing weaknesses oriented 60˚ and 90˚ from the simple shear direction did not show early slip but the new dextral echelon faults often terminated at precut surfaces. This early fault irregularity impact later fault evolution as fault segments reorganized and the system developed a continuous fault surface. Pre-existing weaknesses oriented 120˚ from the simple shear direction exhibited sinistral slip surrounded by distributed dextral shear that facilitate rotation within the shear zone. The cross faults continued to have sinistral slip until they were rotated past 90˚. Within continued strain, new dextral faults developed. Pre-existing weaknesses oriented 150˚ from the simple shear direction exhibited dextral slip and with accumulating of shear strain these faults were replaced by faults more favourably aligned with the applied shear. The experiments with greater early fault trace irregularity required greater strain to develop a mature continuous fault surface, produced greater off-fault deformation and produce wider fault zones. The width of the mature faults are similar to each other, suggesting that mature fault zone width may not reveal the role of early weaknesses on fault evolution. The strike-slip system with sinistral cross-faults had the greatest early fault zone width and also produced the greatest of-fault deformation throughout the fault evolution.

The nature of basal shear and spacing of pre-existing weaknesses impacts the length and overlap of early strike-slip faults that impacts strike-slip fault evolution. The evolution of strike-slip faulting in the experiments with distributed basal shear followed that of the experiments with localized basal shear. The distributed basal shear experiments produced longer initial faults and more irregularly early fault geometries that required greater strain to reach similar stages of fault evolution. While the experiments with wider 5 cm spacing of pre-cut surfaces also showed longer faults, the faults had less overlap with each other. With lesser overlap, the early faults do not impede each other's growth, and the strike-slip system requires lesser strain to reach similar stages of fault evolution.

We show that laboratory experiments using crustal analogue materials that are carefully scaled to simulate faulting deformation within the upper crust can shed insights on the impact and evolution of pre-existing weaknesses on strike-slip faults, like the northwest potion of the 2019 Ridgecrest mainshock rupture. Our results suggest that cross-faults oriented 90˚ from the primary shear may become increasing unfavourably for slip and replaced by slip along more favourably oriented faults aligned with the slip sense of the shear zone. The findings from such experiments can be used to inform future seismic hazards of strike-slip faults with pre-existing weaknesses in the Earth's crust.

https://doi.org/10.5194/egusphere-2026-1948
Preprint. Discussion started: 8 May 2026

Code, data, or code and data availability

Data are available on Figshare at https://doi.org/10.6084/m9.figshare.31961007. Prior to publication we plan to post the dataset within the EPOS data repository.

Author contributions

CRS and MLC together conceptualized the study and CRS performed the experiments, the initial data analysis and original draft preparation. Both CRS and MLC contributed to data analysis and writing.

Competing interests

A declaration of all potential conflicts of interest is required by Copernicus Publications as this is an integral aspect of a transparent record of scientific work. Please see our competing interests policy.

Acknowledgements

This research was partially supported by a NSF grant EAR2040570to MLC, Geological Society of America Graduate Research Grant to CRS and research award to CRS from the University of Massachusetts Amherst department of Earth, Geographic and Climate Sciences.

References

Antoine, S. L., Klinger, Y., Delorme, A., Wang, K., Bürgmann, R., and Gold, R. D.: Diffuse Deformation and Surface Faulting Distribution from Submetric Image Correlation along the 2019 Ridgecrest, California, Ruptures, Bulletin of the Seismological Society of America, 111, 2275–2302, https://doi.org/10.1785/0120210036, 2021.

Bonanno, E., Bonini, L., Basili, R., Toscani, G., and Seno, S.: How do horizontal, frictional discontinuities affect reverse fault-propagation folding?, Journal of Structural Geology, 102, 147–167, https://doi.org/10.1016/j.jsg.2017.08.001, 2017.

Bonini, L., Basili, R., Toscani, G., Burrato, P., Seno, S., and Valensise, G.: The effects of pre-existing discontinuities on the surface expression of normal faults: Insights from wet-clay analog modeling, Tectonophysics, 684, 157–175, https://doi.org/10.1016/j.tecto.2015.12.015, 2016.

Bonini, L., Fracassi, U., Bertone, N., Maesano, F. E., Valensise, G., and Basili, R.: How do inherited dip-slip faults affect the development of new extensional faults? Insights from wet clay analog models, Journal of Structural Geology, 169, 104836, https://doi.org/10.1016/j.jsg.2023.104836, 2023.

Cooke, M. L. and Van Der Elst, N. J.: Rheologic testing of wet kaolin reveals frictional and bi-viscous behavior typical of crustal materials: RHEOLOGIC TESTING OF WET KAOLIN, Geophys. Res. Lett., 39, n/a-n/a, https://doi.org/10.1029/2011GL050186, 2012.

https://doi.org/10.5194/egusphere-2026-1948
Preprint. Discussion started: 8 May 2026

Cooke, M. L., Schottenfeld, M. T., and Buchanan, S. W.: Evolution of fault efficiency at restraining bends within wet kaolin analog experiments, Journal of Structural Geology, 51, 180–192, https://doi.org/10.1016/j.jsg.2013.01.010, 2013.

Crider, J. G. and Peacock, D. C. P.: Initiation of brittle faults in the upper crust: a review of field observations, Journal of Structural Geology, 26, 691–707, https://doi.org/10.1016/j.jsg.2003.07.007, 2004.

Davis, G. H., Bump, A. P., García, P. E., and Ahlgren, S. G.: Conjugate Riedel deformation band shear zones, Journal of Structural Geology, 22, 169–190, https://doi.org/10.1016/S0191-8141(99)00140-6, 2000.

Dooley, T. P. and Schreurs, G.: Analogue modelling of intraplate strike-slip tectonics: A review and new experimental results, Tectonophysics, 574–575, 1–71, https://doi.org/10.1016/j.tecto.2012.05.030, 2012.

Eisenstadt, G. and Sims, D.: Evaluating sand and clay models: do rheological differences matter?, Journal of Structural Geology, 27, 1399–1412, https://doi.org/10.1016/j.jsg.2005.04.010, 2005.

Elston, H., Cooke, M., and Hatem, A.: Non-steady-state slip rates emerge along evolving restraining bends under constant loading, Geology, 50, 532–536, https://doi.org/10.1130/G49745.1, 2022.

Fialko, Y. and Jin, Z.: Simple shear origin of the cross-faults ruptured in the 2019 Ridgecrest earthquake sequence, Nat. Geosci., 14, 513–518, https://doi.org/10.1038/s41561-021-00758-5, 2021.

Freund, R.: Kinematics of transform and transcurrent faults, Tectonophysics, 21, 93–134, https://doi.org/10.1016/0040-1951(74)90064-X, 1974.

González-Muñoz, S., Schreurs, G., Schmid, T. C., and Martín-González, F.: Influence of lateral heterogeneities on strike-slip fault behaviour: insights from analogue models, Solid Earth, 15, 1509–1523, https://doi.org/10.5194/se-15-1509-2024, 2024.

Hatem, A. E., Cooke, M. L., and Madden, E. H.: Evolving efficiency of restraining bends within wet kaolin analog experiments, J. Geophys. Res. Solid Earth, 120, 1975–1992, https://doi.org/10.1002/2014JB011735, 2015.

Hatem, A. E., Cooke, M. L., and Toeneboehn, K.: Strain localization and evolving kinematic efficiency of initiating strike-slip faults within wet kaolin experiments, Journal of Structural Geology, 101, 96–108, https://doi.org/10.1016/j.jsg.2017.06.011, 2017.

Henza, A. A., Withjack, M. O., and Schlische, R. W.: Normal-fault development during two phases of non-coaxial extension: An experimental study, Journal of Structural Geology, 32, 1656–1667, https://doi.org/10.1016/j.jsg.2009.07.007, 2010.

Luyendyk, B. P., Kamerling, M. J., and Terres, R.: Geometric model for Neogene crustal rotations in southern California, Geol Soc America Bull, 91, 211, https://doi.org/10.1130/0016-7606(1980)91%3C211:GMFNCR%3E2.0.CO;2, 1980.

Milliner, C., Donnellan, A., Aati, S., Avouac, J., Zinke, R., Dolan, J. F., Wang, K., and Bürgmann, R.: Bookshelf Kinematics and the Effect of Dilatation on Fault Zone Inelastic Deformation: Examples From Optical Image Correlation Measurements of the 2019 Ridgecrest Earthquake Sequence, J Geophys Res Solid Earth, 126, https://doi.org/10.1029/2020JB020551, 2021.

Nevitt, J. M., Brooks, B. A., Hardebeck, J. L., and Aagaard, B. T.: 2019 M7.1 Ridgecrest earthquake slip distribution controlled by fault geometry inherited from Independence dike swarm, Nat Commun, 14, 1546, https://doi.org/10.1038/s41467-023-36840-2, 2023.

https://doi.org/10.5194/egusphere-2026-1948
Preprint. Discussion started: 8 May 2026

Okubo, K., Bhat, H. S., Rougier, E., Marty, S., Schubnel, A., Lei, Z., Knight, E. E., and Klinger, Y.: Dynamics, Radiation, and Overall Energy Budget of Earthquake Rupture With Coseismic Off-Fault Damage, JGR Solid Earth, 124, 11771–11801, https://doi.org/10.1029/2019JB017304, 2019.

Platt, J. P. and Becker, T. W.: Kinematics of rotating panels of E–W faults in the San Andreas system: what can we tell from geodesy?, Geophysical Journal International, 194, 1295–1301, https://doi.org/10.1093/gji/ggt189, 2013.

Ponti, D. J., Blair, J. L., Rosa, C. M., Thomas, K., Pickering, A. J., Akciz, S., Angster, S., Avouac, J.-P., Bachhuber, J., Bacon, S., Barth, N., Bennett, S., Blake, K., Bork, S., Brooks, B., Bullard, T., Burgess, P., Chupik, C., Dawson, T., DeFrisco, M., Delano, J., DeLong, S., Dolan, J., Donnellan, A., DuRoss, C., Ericksen, T., Frost, E., Funning, G., Gold, R., Graehl, N., Gutierrez, C., Haddon, E., Hatem, A., Helms, J., Hernandez, J., Hitchcock, C., Holland, P., Hudnut, K., Kendrick, K., Koehler, R., Kozaci, O., Ladinsky, T., Leeper, R., Madugo, C., Mareschal, M., McDonald, J., McPhillips, D., Milliner, C., Mongovin, D., Morelan, A., Nale, S., Nevitt, J., O'Neal, M., Olson, B., Oskin, M., Padilla, S., Patton, J., Philibosian, B., Pierce, I., Pridmore, C., Roth, N., Sandwell, D., Scharer, K., Seitz, G., Singleton, D., Smith-Konter, B., Spangler, E., Swanson, B., Jobe, J. T., Treiman, J., Valencia, F., Vanderwal, J., Williams, A., Xu, X., Zachariasen, J., Zimmerman, J., and Zinke, R.: Documentation of Surface Fault Rupture and Ground-Deformation Features Produced by the 4 and 5 July 2019 Mw 6.4 and Mw 7.1 Ridgecrest Earthquake Sequence, Seismological Research Letters, 91, 2942–2959, https://doi.org/10.1785/0220190322, 2020.

Reber, J. E., Cooke, M. L., and Dooley, T. P.: What model material to use? A Review on rock analogs for structural geology and tectonics, Earth-Science Reviews, 202, 103107, https://doi.org/10.1016/j.earscirev.2020.103107, 2020.

Rosa, C. M., Dawson, T., and Kakaria, R.: Surface Rupture Mapping of the 2019 M6.4 and M7.1 Ridgecrest Earthquake Sequence on Lidar and Orthoimagery, 2024.

Schreurs, G.: Experiments on strike-slip faulting and block rotation, Geol, 22, 567, https://doi.org/10.1130/0091-7613(1994)022%3C0567:EOSSFA%3E2.3.CO;2, 1994.

Thielicke, W. and Stamhuis, E. J.: PIVlab – Towards User-friendly, Affordable and Accurate Digital Particle Image Velocimetry in MATLAB, Journal of Open Research Software, 2, https://doi.org/10.5334/jors.bl, 2014.

Toeneboehn, K., Cooke, M. L., Bemis, S. P., Fendick, A. M., and Benowitz, J.: Stereovision Combined With Particle Tracking Velocimetry Reveals Advection and Uplift Within a Restraining Bend Simulating the Denali Fault, Front. Earth Sci., 6, 152, https://doi.org/10.3389/feart.2018.00152, 2018.

Treiman, J. A.: Primary Surface Rupture Associated with the Mw 7.1 16 October 1999 Hector Mine Earthquake, San Bernardino County, California, Bulletin of the Seismological Society of America, 92, 1171–1191, https://doi.org/10.1785/0120000923, 2002.

Wald, D. J. and Heaton, T. H.: Spatial and temporal distribution of slip for the 1992 Landers, California, earthquake, Bulletin of the Seismological Society of America, 84, 668–691, https://doi.org/10.1785/BSSA0840030668, 1994.